Nanoscale

Accepted Manuscript

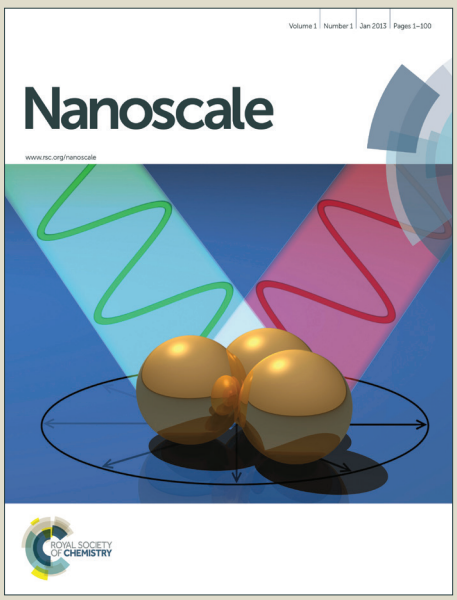

ROYAL SOCIETY OF CHEMISTRY

www.rsc.org/nanoscale

Tailoring Nanoscale Properties of Tungsten Oxide for Inkjet Printed Electrochromic Devices

Pawel Jerzy Wojcik*, Lidia Santos, Luis Pereira, Rodrigo Martins, Elvira Fortunato*

CENIMAT/I3N, Departamento de Ciência dos Materiais, Faculdade de Ciências e Tecnologia, FCT, Universidade Nova de Lisboa (UNL), 2829-516 Caparica, Portugal, Fax: (+351) 21 294 8558, Tel: (+351) 21 294 8562

* Corresponding authors: p.wojcik@campus.fct.unl.pt and emf@fct.unl.pt

Abstract

This paper focuses on the engineering procedures governing the synthesis of tungsten oxide nanocrystals and formulation of printable dispersion for electrochromic applications. By that means, we aim to stress the relevancy of proper design strategy that results in improved physicochemical properties of nanoparticle loaded inks. In the present study inkjet printable nanostructured tungsten oxide particles were successfully synthesized via hydrothermal processes using pure or acidified aqueous sol-gel precursor. Based on proposed scheme, the structure and morphology of nanoparticles were tailored to assure their desired printability and electrochromic performance. Developed nanomaterials with specified structures effectively improve the electrochemical response of printed films resulting in 2.5 times higher optical modulation, and 2 times faster coloration time, when comparing with pure amorphous film.

Keywords: tungsten oxide nanoparticles; electrochromic; hydrothermal synthesis; inkjet printing; nanoelectrochemistry.

1. Introduction

One of the most active trends in material science is the development of inorganic nanoparticles with structural, electrical and optical properties tailored to the specific application. Features of those nanostructures are equally as important as their processability, enabling thin film formation with desired structure and morphology. The combination of these two requirements implies a need for a set of engineering rules combining synthesis and deposition process into one consistent theory.

Some attempts have been made to deposit previously synthesized nanoparticles (NPs) in order to form an electrochromic (EC) film via drop-casting,[1] dip-coating[2] or electrophoretic deposition.[3] In other studies, tungsten oxide nanostructures (WO_X) were grown directly on TCO glass substrate by crystal-seed-assisted hydrothermal synthesis.[4,5] However, obtaining a uniform EC film with good adhesion to the substrate still remains a challenge. Nanostructured WO_X and its hydrates ($WO_X \cdot aH_2O$, $a \in \{1, 1/3, 2\}$) are an important class of materials due to their electrochromic,[4,1] photochromic,[6] photochemical,[7] energy storage[8] and sensing[9–12] properties. Many different approaches have been implemented in order to develop these material using physical vapor deposition (PVD) and wet chemical methods.[13] In recent years, there has been an increasing interest in developing solution-based methods as they offer better control of material morphology while being much less expensive in implementation. From the vast number of existing wet chemical synthesis routes, hydrolysis, condensation, etching and oxidation are the four most relevant.[13] Products of these syntheses which form WO_X polymorphs such as monoclinic,[14] orthorhombic,[2] cubic[15] and hexagonal[16,17] have been reported to exist in various morphological structures depending on precursor composition and process parameters. The impact of crystallographic structure and morphology of WO_X NPs on EC performance have been identified as relevant due to the possible improvement in charge density, coloration efficiency and switching time compared to their amorphous and crystalline counterparts.[18] A size reduction in nanoscale regime also improves chemical, physical, optical and electrical properties due to their large surface area, strong surface adsorption and enhanced band gap.

Among all wet chemical syntheses, hydrothermal treatment seems to be the less complex, cost-effective and well-studied technique, which additionally offers flexibility in possible nanomorphologies. In most studies, precursor for nanostructured WO_X hydrothermal synthesis contain peroxopolytungstic acid (PTA),[19,20] tungstic acid (H_2WO_4),[21] sodium tungstate (Na_2WO_4),[15,9,22] ammonium metatungstate ($(NH_4)_6H_2W_{12}O_{40}$)[7,17] or tungsten hexachloride (WCl_6)[10,11] as a source of tungsten dissolved in aqueous solution, often accompanied by structure directing agent (mainly sulphate based). The acidity of the precursor, and hence the H^+ ions concentration value, was also found to affect crystal WO_X growth during hydrothermal synthesis.[1] Selected precursor is then subjected to hydrothermal conditions, which by definition imply elevated temperature (typically ranging from 120 up to 200 °C) and high vapor pressure

(between 0.21 and 1.73 MPa, respectively; see Section 3 in Supporting Information for more details) for a certain period of time enabling nucleation and growth of crystallites. Besides conventional hydrothermal synthesis in Teflon-lined stainless-steal autoclave, a microwave-assisted variant exists.[16]

Hydrothermal synthesis of water soluble PTA precursor has been also reported to result in NPs of various shapes, varying from flat plates and long rods to round or cubic blocs.[19] It has been proved that process parameters, such as pH value, and residual metal ions have great effect in the crystal size, crystallinity and crystal structure of the obtained product, while the temperature (100 - 200 °C) and precursor concentration are of secondary importance.[15,2] Although the hydrothermal synthesis of WO_X NPs has been widely reported, to our best knowledge, no attempt has been made to deposit those products in a form of printable dispersion.

Likewise, PTA solutions are the most widely used precursors in WO_3 sol-gel film deposition due to their low cost and relatively high stability in an ambient environment. Deposition methods based on sol-gel (PTA) processed EC WO_X such as dip-coating,[23] spin-coating,[10] electrodeposition[24,25] and Inkjet Printing Technology (IPT)[26] offer several advantages over conventional vacuum processed techniques. However, particular attention should be paid to the composition of precursor and processing conditions to get desired microstructure, which would guarantee good performance of EC films.

As it was previously reported by our group,[27,26] the advent of novel wet deposition techniques such as IPT has led to new possibilities in the field of thin solid films based on nanocrystalline metal oxides (MO_X). It was demonstrated that the application of IPT for deposition of MO_X dispersion provides an excellent method for the production of inorganic thin films with controlled composition and microstructure for electrochemical devices, such as dye-synthesized solar cells and EC windows/displays.

Nanocrystalline film is a special category assigned to polycrystalline layers of NPs. Furthermore, the NPs forming the film can be either sintered (mesoporous) or embedded in an amorphous matrix (dual-phase). Figure 1 gives a generalized overview presenting both kinds of NPs loaded printed films for electrochemical applications. From the broad range of available film morphologies used typically in electrochemical applications,[28] only these two are so far feasible in a printing process. Due to the technological limitations, development of *e.g.* vertically aligned ordered nanostructures

or nanoarrays is not possible *via* printing process. Printed mesoporous film shown in Figure 1a, is developed using NPs loaded dispersion, usually stabilized by polymeric additives. Once the dispersion is deposited on a substrate, its liquid components *i.e.* solvents, NPs stabilizers, thickeners, wetting agents and surfactants are no longer needed. Unfortunately, additives typically used to stabilize dispersions of MO_X NPs in a liquid medium are long chain molecules with high evaporation temperatures, which are difficult to eliminate and usually requires high energy to be applied. Such additives may deteriorate or even inhibit electrochemical reaction. The post-treatment process which may include application of elevated temperature or more specific techniques such as photonic pulse curing or UV irradiation is performed in order to form and dry the film, organic burn-out or sintering of NPs. On the other hand, high temperature may affect morphology and microstructure of NPs, due to their thermal instability.[29]

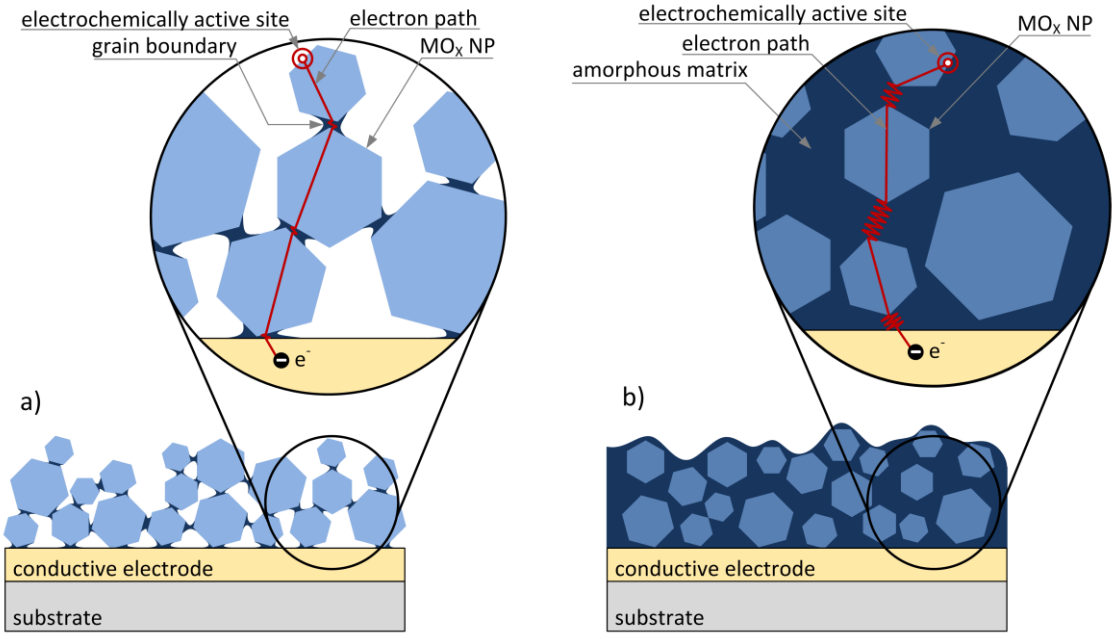

Figure 1. Schematically presented nanocrystalline material for electrochemical applications as a) mesoporous and b) dual-phase films; the electron paths were drawn with respect to their electrical transport properties

As an alternative to energy requiring methods, a dual-phase composition of the film shown in Figure 1b can be induced by mixing NPs with liquid sol-gel precursor, or overprinting the NPs film by sol-gel precursor. Resulting film contains randomly dispersed nanocrystals in a continuous amorphous matrix of the same MO_X, which provides conductive medium for electrons and ions and physically bond the NPs to the surface of the substrate. The sol-gel precursor of WO_3 formulated from

peroxopolytungstic acid requires relatively low temperature of 120 °C for 1 h in order to condensate and densify, resulting in a non-soluble film.[30] The main difference between mesoporous and dual-phase film microstructure lies in character of interconnections between NPs. Randomly oriented NPs are separated by grain boundaries in case of nanocrystalline films or interfacial amorphous regions in dual-phase counterpart. Also the thickness of the printed nanocrystalline electrodes depends of the film morphology. Too thick mesoporous electrode leads to the higher resistance and thus reduction in the efficiency of electrochemical process. In case of dual-phase morphology used in EC devices, two thick films prevent EC action to take place. The optimum thickness is typically around 1 μm in dual-phase *a*-WO_3/WO_X film in EC devices.

This generalized overview shows nanocrystalline material with length scale in all three dimensions which corresponds to quasi-spherical NPs. However, restriction of nanocrystalline regions to one or two dimensions (rod-shaped or layered NPs, respectively) results in an anisotropic charge transport, which is beneficial from electrochemical point of view. Electron transport in elongated shape NPs is much faster than percolation through a network of quasi-spherical crystals.[31] Another aspect is related to the disorder at the interface between neighboring NPs. Regardless of the film morphology, one particular weakness is the presence of a massive number of interfacial boundaries acting as trap sites for electron transport. Such trap limited diffusion lowers overall efficiency of electrochemical device. Grain boundaries in mesoporous films have smaller disorder when comparing with amorphous interface in dual-phase film. However in the second variant, by reducing the NPs size and increasing solid content, the volume fraction of interfacial regions can be significantly reduced.

This paper shows how we can control both, the solution processed synthesis of WO_X NPs and the formulation of printable dispersions. Combination of IPT, NPs synthesis and sol-gel method leads to the development of EC films processed at low temperature, precise patterning with reduced raw material waste, high throughput and flexibility in deposited film composition. The grain size, crystallinity and stoichiometry of NPs incorporated into dual-phase film are dependent only on the origin of those crystals and are defined at the ink formulation stage.[26] This flexibility in material selection not only endows printed devices with a better chemical stability, but it is also responsible for the superior EC performance. Therefore, the versatility of this method makes it an ideal tool for creating materials with predictable and controlled properties, while maintaining their good processability via IPT.

Moreover, in the present work, a facile synthesis of WO_X NPs based on sol-gel precursor with controlled morphology evolution and phase transition under hydrothermal conditions is reported. The structure and morphology of obtained NPs were engineered for their application in IPT and applied in EC device development. The effect of various reaction parameters on crystalline structure, morphology, size, shape, uniformity and agglomeration of NPs leading to variations in EC performance is also described. To the authors' knowledge, no other report on engineering aspects concerning synthesis of metal oxide nanoparticles with predictable and controlled properties combined with printable ink formulation exists.

To assure the desired electrochemical performance and processability, the criteria for NPs size, crystallinity, morphology as well as the uniformity and agglomeration mechanism are given in following sections, providing recommendations on each major technological step and determine constraints, for the application of NPs in printed dual-phase EC films (see Section 1 in Supporting Information for strategy description).

2. Materials and Methods

2.1 Synthesis of WO_X sol-gel precursor

Peroxopolytungstic acid (PTA) was synthesized based on the procedure reported by Tetsuichi Kudo et al.[30] The tungsten metal monocrystalline powder (99.9 %, 0.6-1μm, Aldrich) was carefully added to 50 ml mixture (50:50) of distilled water (Millipore) and hydrogen peroxide (30 %, Sigma-Aldrich). The cooling was employed and the solution was kept slowly stirring in a refrigerator to prevent thermal changes due to the strong exothermic nature of reaction. The excess of tungsten powder was then removed by filtration (0.45 μm syringe filter, Roth) leading to a transparent solution. In order to remove the excess of the hydrogen peroxide, the solution was dried at 65 ºC and washed several times with distilled water. After drying, a water soluble $WO_3 \cdot aH_2O_2 \cdot bH_2O$ orange crystal powder was obtained as final WO_X precursor. The process was optimized to provide high quality of the product and to assure its repeatability by implementation of a very detailed protocol. In order to unify the input material for an ink formulation, products of many syntheses were mixed and grinded together. As the PTA crystals are known for their instability, the final product was stored at low temperature (-18 °C).

2.2 Hydrothermal synthesis of WO_X NPs

For the hydrothermal synthesis, 0.4 g of previously synthesized PTA was dissolved in HCl (37%, Merck) aqueous solution. The final solution was transferred to 23 ml PTFE chamber, set inside a stainless steel autoclave (4745 general purpose vessel, Parr) and installed in the oven (L3/11/B170, Nabertherm) at 180 °C. Approximate value of pressure inside the autoclave during the hydrothermal synthesis is ~1.1 MPa (see Sections 2 and 3 in Supporting Information for more details on hydrothermal synthesis). The HCl concentration (0 M, 0.3 M and 3 M) and the reaction time (2 h, 4 h and 6 h) were selected for each experiment according to determined processes parameters. The product of synthesis was collected by centrifugation at 3000 rpm for 2 min (F140, Focus instruments) and washed three times with distilled water.

2.3 Ink formulation and printing process

The production of dual-phase *a*-WO_3/WO_X films were performed in two separate depositions. Firstly, nanostructured WO_X was used in a form of aqueous (Millipore) alcohol (ethanol 96%, Aga) dispersions in a fixed proportion of 1:1 with a solid content of 0.03 wt%, followed by ultrasonic treatment (UP400S, Hielscher, see Section 7 in Supporting Information for detailed procedure description) and filtering (Roth, 0.45 μm syringe filter). The inks composition results in the viscosity and the surface tension values of 1.5 – 1.75 cP and 20 - 40 mN m^{-1}, respectively, acceptable for conventional office printer. Individual layers (1 cm^2) were repeatedly printed (20-80 passes) using conventional desktop printer (Canon PIXMA IP4850, see Section 4 in Supporting Information for detailed printing system description) in regular intervals of around 1 min while being exposed to a relative humidity of 50 %, at 28 ºC on ITO PET substrates (Sigma-Aldrich, 1000 Å of ITO, 60 Ω/sq, T > 75 % at 550 nm, see Sections 5 and 6 in Supporting Information for more details concerning substrate preparation). Variable numbers of passes depending on the solid content nature were adjusted separately in order to obtain uniform coverage. All films were dried at room temperature for several hours. Secondly, 0.16 g of PTA was dissolved in 0.92 g of water and 0.92 g of alcohol (ethanol 96%, Aga). The solution was stirred for 15 minutes, 150 rpm at 60 °C and filtered (Roth, 0.45 μm syringe filter). Individual layers (1 cm^2) were printed only once under equal environmental conditions on top of the previously

deposited NPs. All films were dried at room temperature for 24 h and annealed in air at 120 °C (EHRET, TK4067, Germany) for 1 h.

2.4 Characterization

The morphological and structural characterization of WO_X NPs was performed by SEM (Auriga SEM-FIB, Zeiss) and XRD (XPert PRO, PANalytical). Supplementary structural characterization of WO_X NPs was performed by FT-IR (Nicolet 6700, Thermo Electron Corporation). Thermal analysis of NPs was performed by Thermogravimetric Analyzer (STA 449 F3 Jupiter, Netzsch) in air with a heating ramp of 5 °C/min starting from RT up to 600 °C. Intrinsic viscosity of an ink vehicle and genuine CANON inks was measured by glass capillary viscometer (CANNON-UBBELOHDE, 9721-K53 CUC Series). Surface tension was measured with glass stalagmometer (Rohr A, NEUBERT-GLAS). Optical measurements of printed dual-phase films were performed *in-situ* using a spectrometer set-up consist of HR4000 High-Resolution Spectrometer (Ocean Optics), Halogen Light Source HL-2000-FHSA (Mikropack) in range of 450-850 nm (optical response was measured at λ = 800 nm). The electrochemical cell consisting of working electrode (dual-phase EC film) and platinum wire used as counter electrode was filled with lithium based gel electrolyte prepared according to the recipe described elsewhere.[32] The EC cell was driven by High Current Source Measure Unit (KEITHLEY 238) using a square wave (±2 V, 30 s per pulse) and a linear stair pulse (from -2 V up to 2 V in a 0.5 V step, -2 V of bias, 30 s per pulse) modes in order to induce EC modulation. Spectra were recorded in reference to the uncoated substrate under equal conditions (see Section 8 in Supporting Information for detailed system description).

3. Results and discussion

3.1. Structure, morphology and printability of synthesized WO_X NPs

There are only few studies reported in literature wherein the effect of various reaction parameters on crystalline structure and morphology of NPs leading to variations in EC performance have been described.[4,1] Results presented in this section show how the structure and morphology of WO_X NPs can be simply tailored by adjusting the pH of the precursor in the hydrothermal reaction system. Figure 2a shows the XRD patterns of the as-synthesized WO_X nanopowders prepared at various acidities

and reaction time with corresponding Inorganic Crystal Structure Database (ICSD) references.

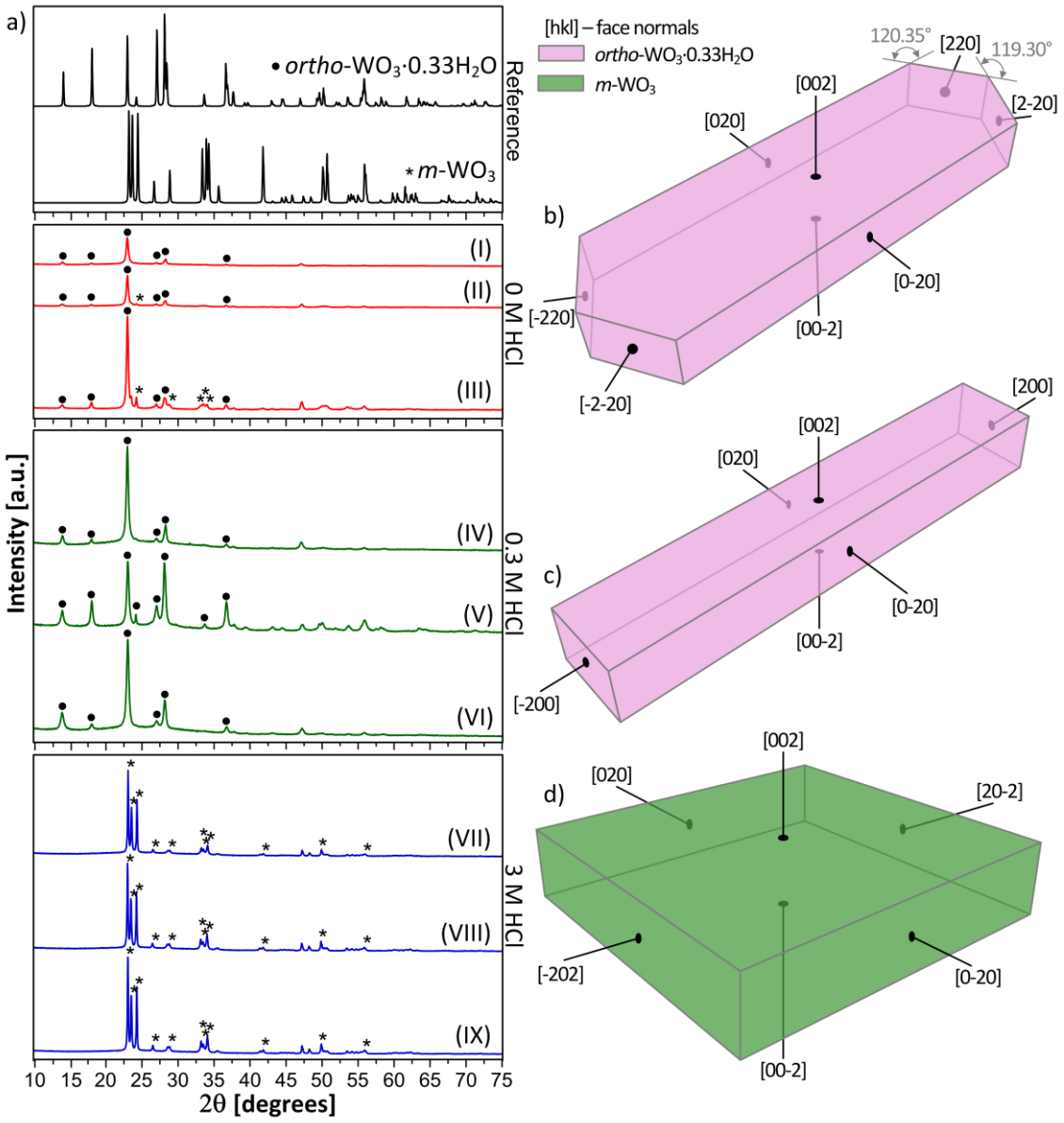

Figure 2. a) XRD difractograms of nanopowders obtained via hydrothermal syntheses performed from (I) non-acetified precursor solution after 2 h, (II) 4 h and (III) 6 h; (IV) precursor dissolved in 0.3 M HCl after 2 h, (V) 4 h and (VI) 6 h; (VII) precursor dissolved in 3 M HCl after 2 h, (VIII) 4 h and (IX) 6 h; reference spectra for *ortho*-$WO_3 \cdot 0.33H_2O$ (ICSD: 98-003-7822) and *m*-WO_3 (ICSD: 98-009-1587) have been placed above; 3D models (isomeric projections) of b,c) *ortho*-$WO_3 \cdot 0.33H_2O$ nanorods and nanowires, d) *m*-WO_3 nanoslabs/nanoplates developed based on quantitative information concerning the preferential crystalline orientation (texture coefficient) and SEM observations

The products of syntheses performed from non-acetified precursor solution indicate the coexistence of two WO_X polymorphs, namely monoclinic (*m*-WO_3) and orthorhombic tungsten oxide hydrate (*ortho*-$WO_3 \cdot 0.33H_2O$). Lowering acidity of precursor by dissolving PTA in 0.3 M HCl and 3 M HCl causes phase unification to *ortho*-$WO_3 \cdot 0.33H_2O$ and *m*-WO_3, respectively. The enhancement in lithium ion diffusion rate, and hence shorter electrochemical response is expected for films containing orthorhombic hydrate (*ortho*-$WO_3 \cdot 0.33H_2O$) NPs due to the higher electronic conductivity of this phase when comparing to monoclinic (*m*-WO_3) nanocrystals.[33] Therefore, the product of synthesis from PTA dissolved in 0.3 M HCl seems to be the most desirable, as long as the crystallinity is concerned.

Fourier Transform Infrared Spectroscopy and Simultaneous Thermal Analysis (see Section 12 and 13 in Supporting Information for corresponding spectra and discussion) used to indicate coordinated water content in nanopowders, confirmed results obtained by XRD. As expected, high amount of water has been observed in the powder synthesized from non-acetified precursor and precursor dissolved in 0.3 M HCl. Furthermore, no indicators of water have been detected in the powder synthesized from the precursor dissolved in 3 M HCl indicating its anhydrous nature.

3D projections of orthorhombic tungsten oxide hydrate NPs presented in Figures 2b, 2c and monoclinic tungsten oxide NP presented in Figure 2d were drawn using quantitative information concerning the preferential crystalline orientation obtained on a basis of texture coefficient, and SEM observations (see Sections 10 and 11 in Supporting Information for detailed description of 3D model development). Schemes of both *ortho*-$WO_3 \cdot 0.33H_2O$ nanorods and nanowires are oriented in the same way. However, facets (220), (-220), (2-20) and (-2-20) do not constitute the shape of NP synthesized from precursor dissolved in 0.3 M HCl. These facets disappear due to the dominant growth of NP in [200] and [-200] directions, whilst slower growth along [020] and [0-20].

SEM micrographs of the as-synthesized WOx NPs prepared at different acidity and reaction time are shown in Figure 3. The imminent difference obvious at a glance between the morphological characteristics of WO_X NPs synthesized at various precursor acidities is a distribution and shape of nanostructured particles in a form of nanoslabs, nanoplates, nanorods and nanowires. According to micrograph presented in Figures 3a-3c, the syntheses performed from non-acetified precursor solution result in a mixture of

agglomerated nanorods and rectangular nanoplates previously identified by XRD analysis as *ortho*-$WO_3 \cdot 0.33H_2O$ and *m*-WO_3 tungsten oxide polymorphs, respectively.

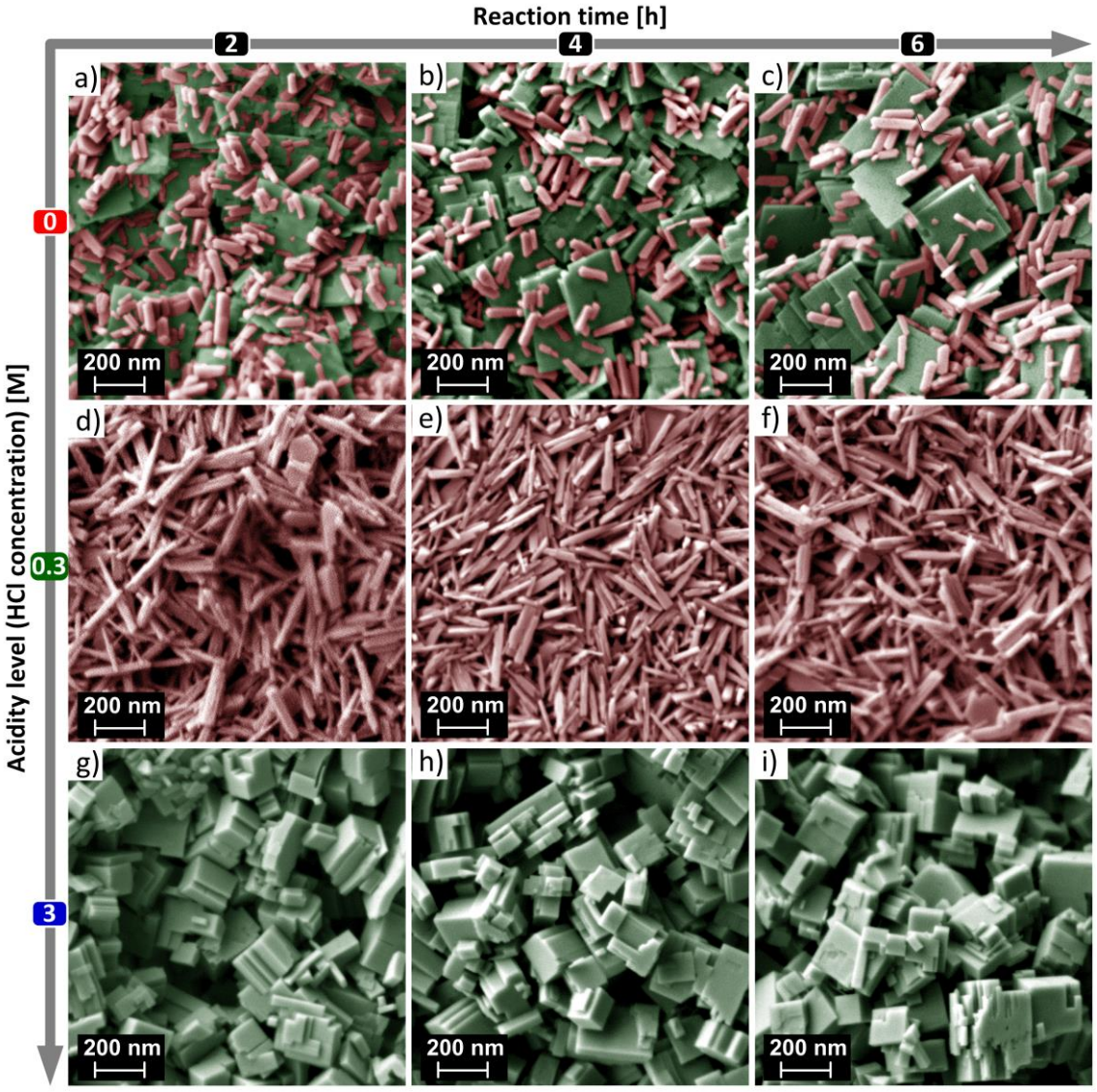

Figure 3. SEM images of nanostructured products obtained via hydrothermal syntheses performed from a) non-acetified precursor solution after 2 h, b) 4 h and c) 6 h; d) precursor dissolved in 0.3 M HCl after 2 h, e) 4 h and f) 6 h; g) precursor dissolved in 3 M HCl after 2 h, h) 4 h and i) 6 h; micrographs were false colored for enhancing visual illustration

The agglomeration of *m*-WO_3 nanoslabs is ordered in multilayer stacks and proceeds with time, while the agglomeration of *ortho*-$WO_3 \cdot 0.33H_2O$ NPs seems to be limited by decreasing quantity of this phase with elapsed reaction time. Such phase transition from orthorhombic to monoclinic under similar conditions was observed also by Jiayin et al.[34] Powders prepared from PTA dissolved in 0.3 M HCl shown in Figures 3d-3f are composed of *ortho*-$WO_3 \cdot 0.33H_2O$ well-defined cubic nanowires with slight

but progressive agglomeration, which is privileged along the rod's faces of larger area. It is therefore an argument to challenge common opinion[35] saying that sulfates are necessary as directing agents for the formation of 1D WO_3 nanostructures. Powders prepared from PTA dissolved in 3 M HCl shown in Figures 3g-3i are composed of *m*-WO_3 nanoslabs which agglomerate with the reaction time to multilayer stacks leading to formation of cubic structures. The resulting polyhedrons, despite big differences in dimensions, own smooth surfaces and well-defined corners of 90 °.

In order to reduce the complex visual information contained in SEM images to easily interpretable quantitative information, the micrographs shown in Figure 3 can be presented in a form of histograms as shown in Figure 4. The dimensions were estimated by measuring the size (length) of randomly selected particles in enlarged SEM images. Such analysis of the SEM micrographs revealed discrete histograms shown in Figure 4a, 4c and 4e, to which Gaussian curves were fitted to present continuous particle size distribution.

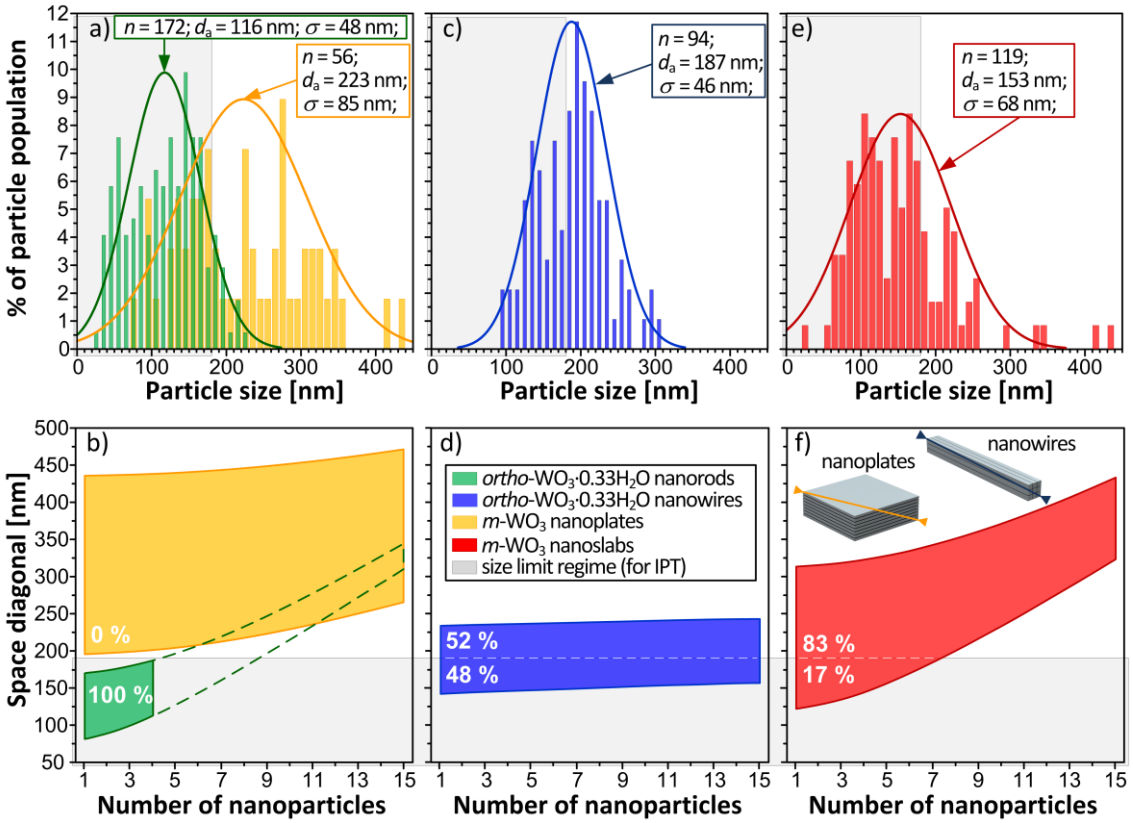

Figure 4. Discrete (histogram) with continuous (Gaussian) particle size distribution and corresponding agglomerate size estimation for products of 6 hours long syntheses performed from a, b) non-acetified precursor solution (agglomerates of nanorods with number of NPs higher than four were not observed), c, d) precursor dissolved in 0.3 M

HCl and e, f) precursor dissolved in 3 M HCl; particle size was defined as the largest dimension measured along the NP; parameters n, d_a and σ stand for number of NPs in a population, arithmetic mean particle size and standard deviation, respectively; agglomerate size is defined as its space diagonal and uniform size distribution of agglomerates is assumed.

Products of syntheses from non-acetified precursor solution present bimodal distributions. The *ortho*-$WO_3 \cdot 0.33H_2O$ nanorods (Figures 3a – 3c and Figure 4a) are 116±48 nm long, ~40 nm wide and ~20 nm thick, while the *m*-WO_3 nanoplate fraction of the same product have uniform thickness of ~12 nm with other dimensions varying in size of 223±85 nm. The *ortho*-$WO_3 \cdot 0.33H_2O$ nanowires prepared from PTA dissolved in 0.3 M HCl (Figures 3d - 3f and Figure 4c) are 187±46 nm long, having well-defined square cross-section with a side length of ~12 nm. The *m*-WO_3 cubic structures prepared from PTA dissolved in 3 M HCl (Figures 3g – 3i and Figure 4e) are agglomerates of rectangular nanoslabs with uniform thickness of ~20 nm while other dimensions vary in size of 153±68 nm.

Synthesized NPs must comply with size limitation in order to allow its usage in inkjet printable inks. It can be assumed (with some exceptions *e.g.* nanowire alignment in a microfluidic flow[36,37]) that the maximum particle size should be 50-100 times smaller than nozzle diameter. According to the print-head specification (Canon Thermal DOD FINE^{TM}) used in Canon PIXMA IP4850 printer, the nozzle diameter is 9 μm. Therefore, not all nanostructured products obtained in experiments comply with size limitations (particle size ≤ 180 nm), even when assuming that agglomeration does not occur (see Figures 4a, 4c and 4e). Based on plots shown in Figure 4b, 4d and 4f it is possible to conclude that nanorods synthesized from non-acidified precursor and PTA dissolved in 0.3 M HCl are printable in 100 % and 48 %, respectively (under assumption of uniform size distribution of agglomerates, and cluster size not exceeding 15 NPs). Nanoplates synthesized from non-acidified precursor are not printable at all, and only 17 % of the ones synthesized from PTA dissolved in 3 M HCl are capable to pass the nozzle. Therefore, NPs agglomeration has dramatic influence on nanostructure printability in case of nanoplates and nanoslabs, while in case of nanorods and nanowires seems to not be that relevant. Thus, the major concern is associated with the nanoplates, as they are relatively large in size and tend to agglomerate significantly

exceeding size limitation for this particular Canon printing system. These results indicate that the use of appropriate acidity of the precursor influences the nucleation and growth of WO_X NPs under hydrothermal conditions, and thus the product may be tailored to specific sizes and shapes.

There are two critical requirements for ink in the area of printed electronics. Firstly, the ink must ensure reliable print under deposition conditions. Secondly, printed film must display required functional performance. In general, NPs loaded inks are two phase fluids consisting of a dispersion of nanocrystals in a liquid carrier (aqueous or organic), so-called vehicle. The viscosity of such suspension depends on the NPs volume fraction, their shape expressed usually by aspect ratio (length/width) as well as particle orientation in a fluidic flow, which may imply critical consequences especially when the printing process is concerned.[38] Thus, the development of printable functional inks is strictly reliant on the development of nanoparticles. Thereby, the key issue is to synthesize product with morphology tailored to assure desired physical properties of its suspension, on which several constraints are imposed. Typically, viscosity is in the range of 1-20 cP depending on printing system used and the surface tension value between 30 and 40 mN m^{-1} (see Section 7 in Supporting Information for more details on tailoring viscosity and surface tension of the ink).

Irrespectively of the complexity of an ink vehicle, controllable and reproducible deposition of NPs-loaded inks encompasses some challenges. In standard desktop printers, such as CANON PIXMA IP4850 used in present studies, the jetting parameters can be controlled only by proper adjustment of ink fluid parameters, as there is no direct access to the print-head's driver. To assure proper droplets formulation, the custom ink should have similar rheology to the genuine CANON inks (indicated in Figure 5). In the same time it should be water-based ink as most of the organic solvents may dissolve printhead structure. Such water-based ink offers several advantages: (i) reduced volatility, (ii) low reactivity with the substrate and print-head elements and (iii) fewer restrictions in terms of safe handling when comparing with organic solvents based counterparts. In order to adjust the viscosity and surface tension to the range within which the printer operates, the ethanol weight fraction was selected as 0.5, according to the plot shown in a Figure 5, resulting in values of 2 cP and 27 mN m^{-1}, respectively. The viscosity of obtained vehicle is too high when comparing with genuine CANON inks, but addition of NPs in amount of 0.03 wt%, or 8.7 wt% of PTA transfers the

viscosity value into CANON inks regime. Thus, the viscosity and the surface tension of both, NPs dispersion and WO_3 sol assure expected printability.

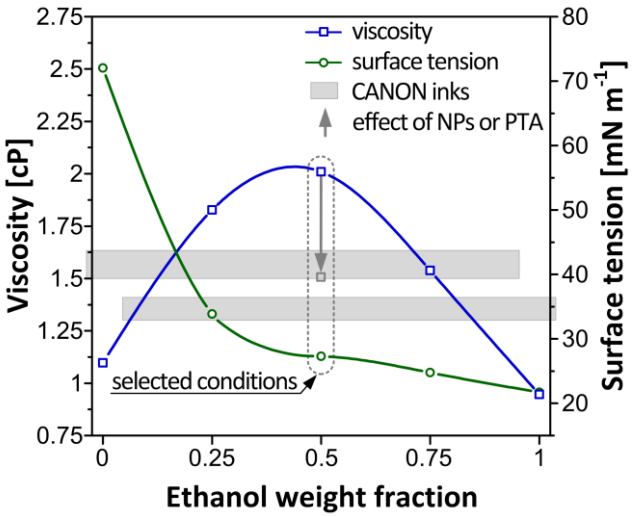

Figure 5. Viscosity and surface tension of an alcohol aqueous ink vehicle as a function of ethanol weight fraction; the regime of genuine CANON inks (CLI-526 cyan, magenta and yellow) is shown in grey

Once the ink is deposited on a substrate, its liquid components *i.e.* solvents, NPs stabilizers, thickeners, wetting agents and surfactants are no longer needed. Unfortunately, additives typically used to stabilize dispersions of NPs in a liquid medium are long chain molecules with high evaporation temperatures, which are difficult to eliminate and usually requires high energy to be applied. Such additives may deteriorate or even prohibit electrochemical action. The post-treatment process which may include application of elevated temperature or more specific techniques such as photonic pulse curing or UV irradiation is performed in order to form and dry the film, organic burn-out or sintering of NPs. On the other hand, high temperature may affect morphology and microstructure of NPs, due to their thermal instability.[29]

3.2. Film morphology

The fabrication of inkjet printed EC films were performed via two separate depositions, according to the diagram presented in Figure 6a. Firstly, printable WO_X dispersion was deposited on the substrate and dried. Secondly, such nanocrystalline film was coated with printable sol, containing precursor of WO_3, resulting in dual phase *a*-WO_3/WO_X film. Depending of the NPs incorporated to the dispersion in the first deposition step, dual-phase *a*-WO_3/*m*-WO_3, *a*-WO_3/*ortho*-$WO_3 \cdot 0.33H_2O$ or *a*-WO_3/(*m*-

WO_3 + *ortho*-$WO_3 \cdot 0.33H_2O$) compositions were obtained. The existence of amorphous phase (*a*-WO_3) in each film under investigation provides compact mechanical structure of the film and guarantees EC effect, by allowing electronic conduction to take place in the structure processed at low temperature. The use of PTA as the precursor for NPs synthesis and a-WO_3 coating shows convergence of the technologies. A uniform coverage of nanocrystals by amorphous coating was confirmed by SEM micrograph presented in Figure 6b in which nanowires are randomly dispersed in a single level pattern embedded in continuous amorphous film.

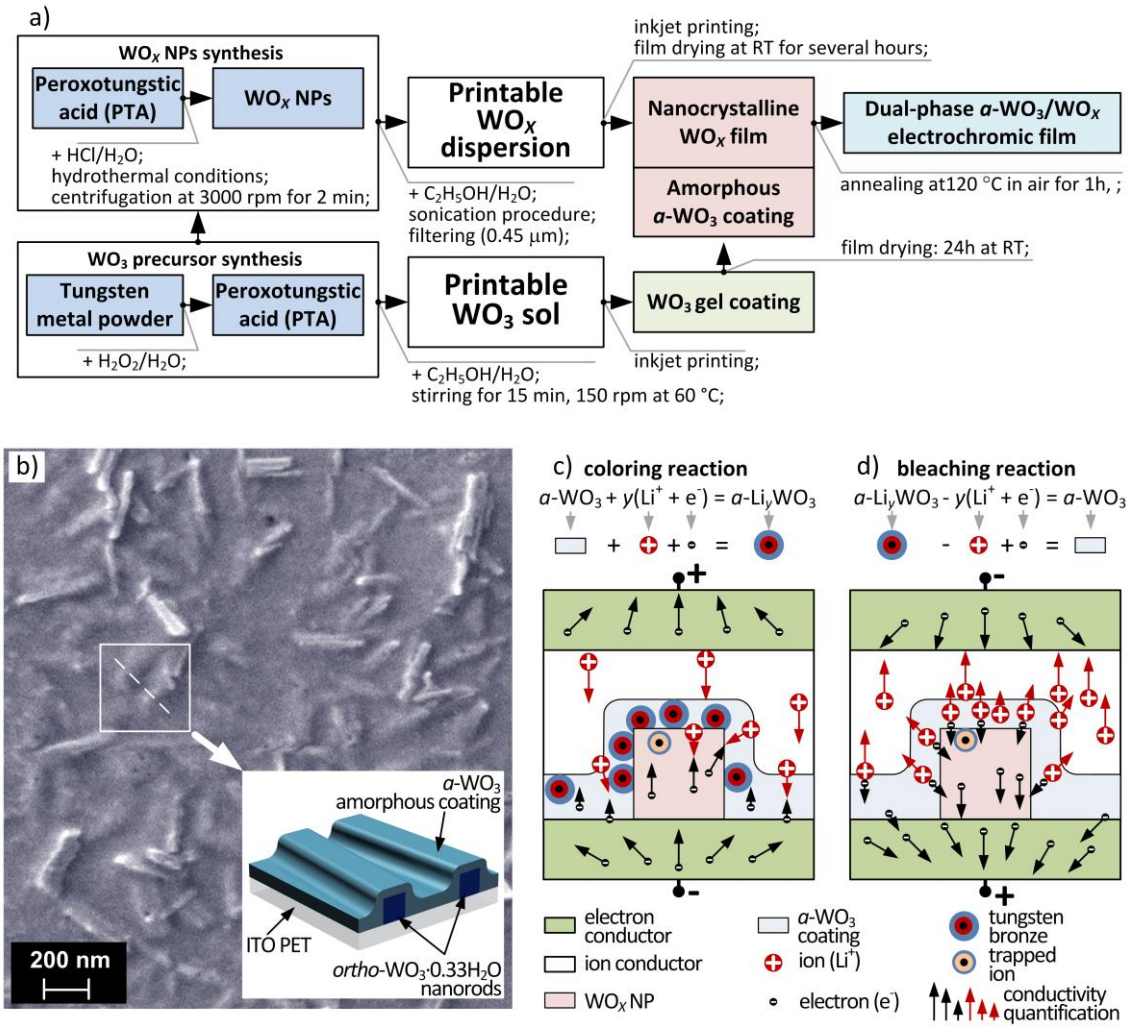

Figure 6. Dual-phase *a*-WO_3/WO_X EC film in a) a schematic diagram representing the elements of the studied material system with corresponding technological steps, b) SEM image of *a*-WO_3/*ortho*-$WO_3 \cdot 0.33H_2O$ on ITO PET substrate (inset: schematic representation) and schematic illustration of c) coloring and d) bleaching reaction under operational conditions

3.3. Electrochromic response of inkjet printed films

According to the electrochromism theory, the mechanism of optical modulation is different in crystalline and amorphous phase. In nanocrystalline WO_X electrochromism arises due to the increasing Drude type (metallic) reflection, observed especially in IR region with increasing free electron/lithium injection.[39] On the other hand, in amorphous phase, the most widely accepted model assumes that the optical modulation upon the double injection occurs through increasing absorption arising from the transfer of localized electrons between W^{5+} and W^{6+} sites, so called small polaron absorption.[40–42] Figure 6c and 6d show generalized mechanism of electrochemical reaction in EC device based on dual-phase film for coloring and bleaching, respectively. It is assumed that EC WO_3 film in transparent state can be switched reversibly to a colored state by both insertion of ions and electrons to form tungsten bronze (a-Li_yWO_3, where y is the fractional number of sites filled in the WO_3 lattice). Although being an obvious oversimplification, presented schemas provide very convenient background for further discussion on a-WO_3/WO_X electrochemical performance. In considered device structure, an EC film is in contact with ion (Li^+) conductor, which also serves as ion storage. Two electron (e^-) conductors serve for setting up the distributed electric field. Operational voltage shuttles ions into and out of the film causing coloring (a-Li_yWO_3) and bleaching (a-WO_3) action, respectively. Nanostructured WO_X is more conductive for e^- and less conductive for Li^+ ions when comparing to a-WO_3. Therefore, the highest density of optically active centers is in the interface between WO_X and a-WO_3, where electrons meet ions leading to the formation of a-Li_yWO_3. Despite slower Li^+ diffusion in crystalline medium, some ions cross the grain boundary and get trapped into the crystalline structure of NP, due to the existence of imperfections.

Nanocrystalline or NPs loaded dual-phase films provide a high surface area for electrochemical reaction, effective diffusion of ions into the interface/surface, high transparency in a visible range and sufficient electronic conductivity. Ion-intercalation reaction is strongly dependent of chemical and crystallographic structure of MO_X, while ion diffusion coefficient and the length of diffusion path depend on NPs microstructure.[43,44] The smaller NPs dimensions, the shorter diffusion path length. On the other hand, high electronic conductivity of crystalline phase leads to the enhancement in lithium ion diffusion rate. The electronic conductivity of stable WO_X NPs was reported to be the highest for orthorhombic hydrate ($ortho$-$WO_3 \cdot 0.33H_2O$) and gradually smaller for sub-stoichiometric (WO_{3-y} where $0 \leq y \leq 3$), monoclinic (m-WO_3)

and hexagonal (*h*-WO_3) structure, respectively.[33] The high charge carrier concentration in anhydrate WO_{3-y} ($0 \leq y \leq 3$) is explained by non-stoichiometry, where the free electrons are balanced by much less mobile oxygen vacancies. Both, conduction phenomena assure efficient charge compensation during the redox process and hence improve switching kinetics of EC films. When size of NPs dispersed in a film decreases, the trapping and scattering effect of free charge carriers on grain boundaries lead to higher film resistivity. If the size of NPs is smaller than electron mean free path, the scattering on grain boundaries dominates and the advantage of dual-phase composition is becoming negligible.

Quantitative EC response analysis is based on CA technique which is a square-wave potential step method coupled with optical spectroscopy used for analysis of switching kinetics and contrast of the film. The electrochemical cell consisting of working electrode (printed film on ITO PET substrate) and platinum wire used as counter electrode was filled with lithium based gel electrolyte prepared according to the recipe described elsewhere.[32] Resulting cell was driven by power supply in order to induce EC modulation in a linear stair pulse mode (from -2 V up to 2 V in a 0.5 V step, -2 V of bias, 30 s per pulse). Spectra were recorded in reference to the uncoated substrate under equal conditions. The main output is confined to the basic performance indicators consisting of change in optical modulation (ΔOD), coloration time (τ_{col}), bleaching time (τ_{bl}) and site saturation effect ΔT_{SS} (see Section 9 in Supporting Information for definitions of parameters). Comparison between corresponding changes in optical densities of dual-phase films in reference to the response of pure amorphous film is shown in Figure 7a.

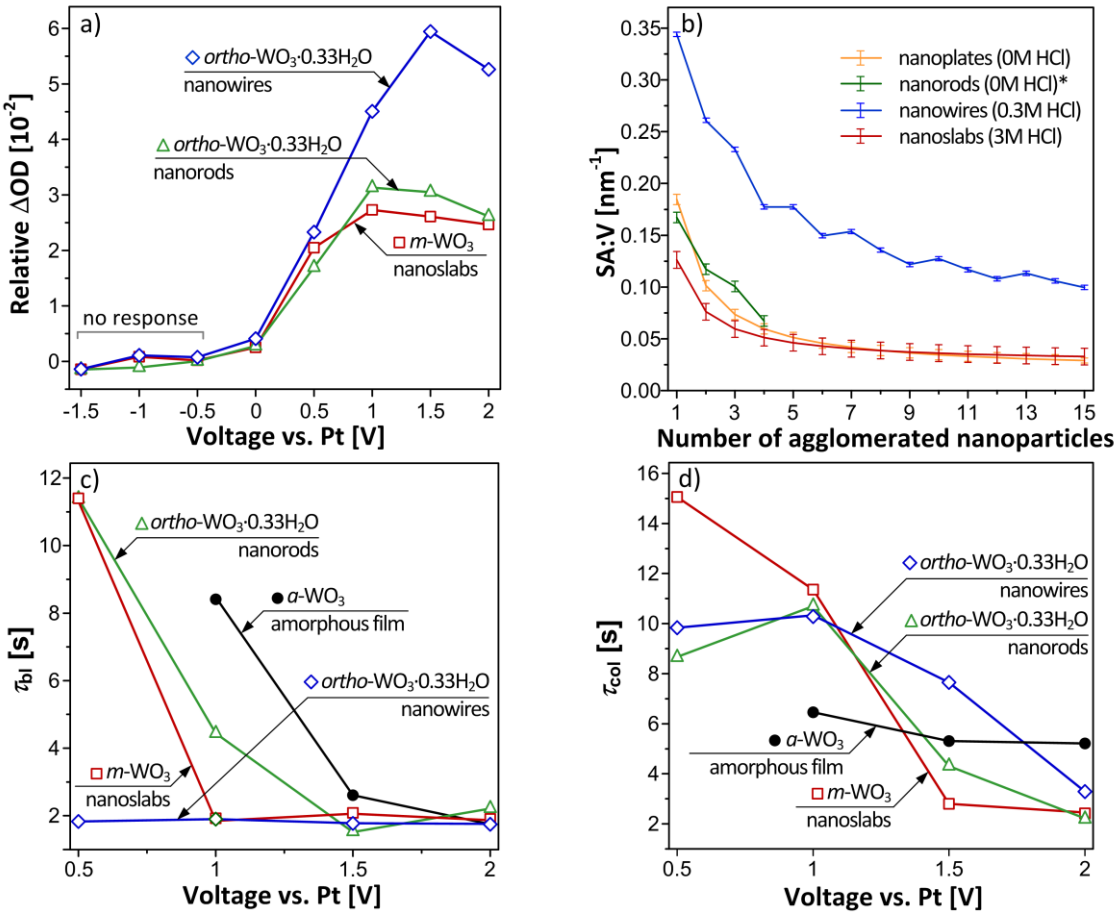

Figure 7. Plots showing a) change in optical density (ΔOD) as a function of operating voltage for dual-phase inkjet printed films containing different types of NPs (relative values represent the difference between ΔOD of dual-phase film and ΔOD of pure amorphous analog), b) an estimation of SA:V as a function of agglomerate size, based on particle size distribution for products of 6 hours long syntheses; y-axis error bars reflect standard deviation of a mean particle size; *agglomerates of nanorods (synthesized from PTA dissolved in 0M HCl) with number of NPs higher than four were not observed, c) variation in bleaching time for dual-phase inkjet printed films containing different types of NPs (bleached state was restored by supplying -2 V, after coloring under operational voltage; amorphous film is presented for comparison), and d) variation in coloring time as a function of operating voltage for dual-phase inkjet printed films containing different types of NPs (amorphous film is presented for comparison)

Such presentation of the optical modulation provides the information regarding the role of NPs content selectively, in EC mechanism. Films which contain either *ortho*-

$WO_3 \cdot 0.33H_2O$ or *m*-WO_3 NPs, outperform their amorphous analogs in term of optical modulation (see Section 16 in Supporting Information for corresponding spectral responses). It is a consequence of dual-phase microstructure which provides large interfaces between dual-phase film and gel electrolyte, as well as between amorphous and nanocrystalline phases itself. NPs are known to have large specific surface area therefore their properties are dominated by the surface rather than by the bulk. Nanostructured MO_X NPs with large specific surface area enhance EC performance of printed dual-phase films in two different ways. Firstly, in terms of optical modulation, higher values will be obtained by increased interaction with lithium ions due to the higher active surface area. The EC reaction occurs in electrochemically active sites, hence the higher the number of active sites available, the strongest reaction will occur. Secondly, amorphous phase combined with nanocrystalline content results in light and easily penetrable for cations medium. Such microstructure promotes ion diffusion through the porous film. The highest ΔOD values were recorded for film containing *ortho*-$WO_3 \cdot 0.33H_2O$ nanowires, which is a direct repercussion of the highest value of SA:V for those NPs, even in spite of progressing agglomeration leading to the formation of massive block, significantly reducing specific surface area (see Section 14 in Supporting Information for model of agglomeration for various regular shaped NPs). Size distributions of synthesized products were used to estimate SA:V as a function of agglomerate size, shown in Figure 7b. The highest values of SA:V were obtained for agglomerates of *ortho*-$WO_3 \cdot 0.33H_2O$ nanowires prepared from PTA dissolved in 0.3 M HCl. Their individual specific surface area is also the highest among synthesized products. The least favorable in terms of SA:V are *m*-WO_3 nanoslabs synthesized from PTA dissolved in 3 M HCl, irrespectively of the agglomerate size. Obtained SA:V estimations stay in agreement with theoretical considerations (see Figure S21 in Supporting Information). Therefore, synthesized *ortho*-$WO_3 \cdot 0.33H_2O$ nanowires are the most desirable products in terms of SA:V, as long as their electrochemical application is concerned.

It should be noted that the performance of EC films either amorphous, nanocrystalline or dual-phase, in particular ΔOD, is ultimately governed not only by the film composition but also by the thickness (see Section 15 in Supporting Information for details concerning dependence between film thickness and EC response).

Differences in switching dynamics of dual-phase and amorphous films shown in Figure 7c and Figure 7d, provide an information regarding the role of NPs in the

dynamics of the EC reaction. Low potentials applied between electrodes (0.5 V and 1 V) cause slow but apparent transition between bleached and colored state. However, the rate of the electrochemical reaction is lower when comparing with pure amorphous phase. Operation with the higher voltage level (1.5 V and 2 V) results in improved coloration time (< 3 s for 2 V) of all films containing NPs in comparison with pure amorphous film (~5 s). The application of a reverse potential (-2 V) restores the film to its bleached state over a short period of time denoted as τ_{bl}. The switching dynamics from colored to bleached state depends on the voltage level at which coloration was induced.

According to Figure 7d when restoring the pure amorphous film after coloration at low potential (1 V), the optical change proceeds very slowly (~8.5 s). However, bleaching period is much shorter in case of dual-phase films. Films containing *ortho*-$WO_3 \cdot 0.33H_2O$ nanowires bleach within time lower than 1.9 s, irrespectively of the level of the operational voltage which induced coloring state, owed to high electronic conductivity of those nanostructures. For other films, NPs content is beneficial especially when low voltage levels are used to supply the device. The coloration kinetics is observed to be slower than bleaching kinetics for all the films under investigation, which stays in agreement with the well-defined, but different mechanism governing the two processes. While the exchange of the current density at the EC film-electrolyte interface controls coloration kinetics, the space charge-limited Li^+ ion diffusion current governs the bleaching time.[41]

Presented results shows beneficial impact of WO_X NPs on EC performance of printed films, reflected in 2.5 times higher optical modulation, and 2 times faster coloration time, when comparing with pure amorphous film. Such improvement is mainly attributed to higher interface between amorphous and nanocrystalline phase, as well as between MO_X layer and ion conductor. The impact of NPs selection on reversibility of printed dual-phase EC films is demonstrated in Figure 8, which represents so called site saturation effect.[45] When the operational voltage exceeds a certain value, the transmittance of the bleached films is markedly lower than its value before coloration which means that the device does not bleach completely ($\Delta T_{ss} > 0$). The EC action was fully reversible for films containing *ortho*-$WO_3 \cdot 0.33H_2O$ NPs, while films with other phases did not bleach completely due to the intensive charge trapping particularly evident for films containing *m*-WO_3 phase. This irreversible deterioration in

m-WO_3 phase may be caused by lattice strain and possible crystal distortion which affect the Li^+ ion insertion/extraction. It was also observed that the addition of *ortho*-$WO_3 \cdot 0.33H_2O$ NPs to the film lowers the charge trapping effect in the amorphous phase due to increased surface area of *a*-WO_3 matrix. Moreover, *ortho*-$WO_3 \cdot 0.33H_2O$ NPs contain coordinated water and are also hydrophilic, what makes the films with high nanocrystalline content more hydrated. Such physisorbed water gives the significant enhancement in ion dynamics through an amorphous phase.[41]

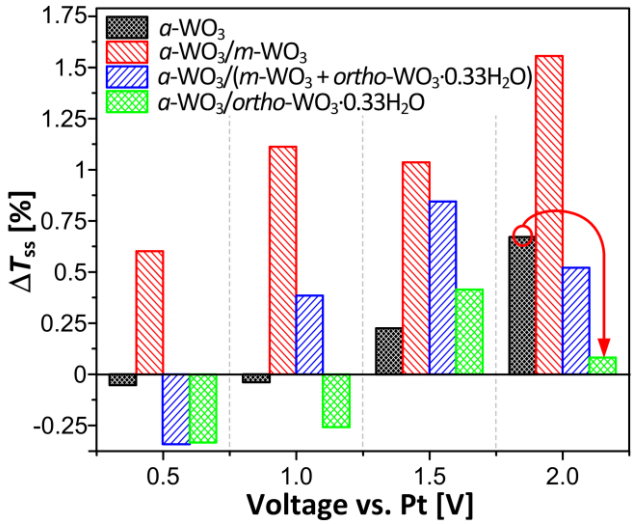

Figure 8. Variation in site saturation effect (ΔT_{SS}) as a function of operating voltage for dual-phase inkjet printed films containing NPs synthesized in 6 h long process ($\Delta T_{SS} = 0$ for fully reversible optical effect)

3.4. Design rules outline

Figure 9 summarizes engineering rules applied in WO_X NPs synthesis and ink formulation. Following the indications marked as preferable area, assures good printing processability and enhancement in performance of *a*-WO_3/WO_X film when comparing to pure amorphous microstructure. In order to determine such preferable regime for EC applications, each alternative was studied until the choice is clear, rational and optimal according to existing knowledge. Such design rules outline is an approach to proper arrangement of various factors including structural, morphological, electrical and rheological properties while taking into account post-treatment conditions. However, those eleven parameters do not restrict the scope of research in this area. Many other factors may be considered as relevant, depending on the studies complexity.

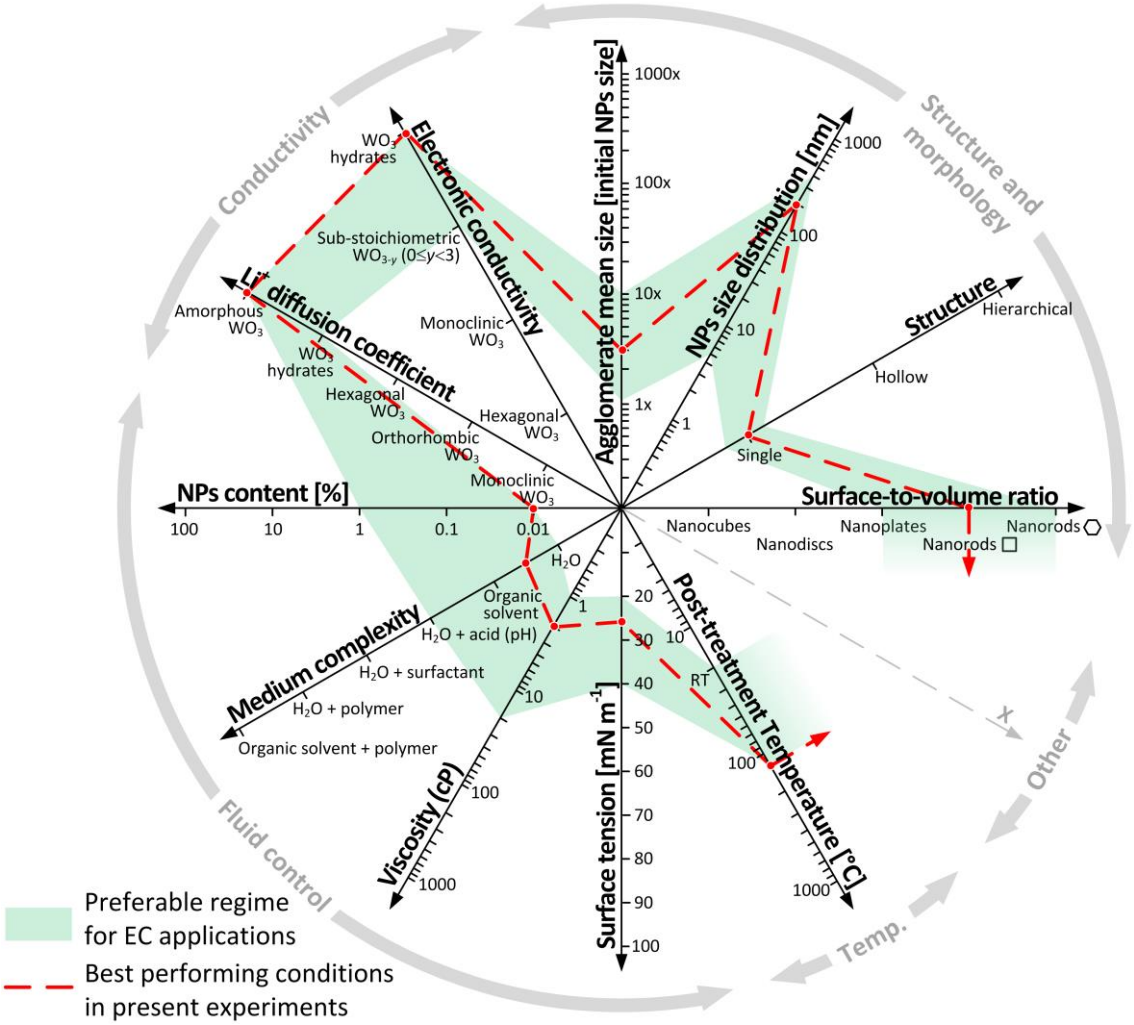

Figure 9. The design rules outline for WO_X NPs synthesis and ink formulation process; preferable regime for EC applications based on inkjet printed inorganic films and factors for best performing material in present studies were also plotted

The rules formulated in the present studies relate to WO_X engineering for EC applications, but it should be noted that the same constrains are applicable for other applications based on this material. Therefore, the versatility of this method makes it an ideal tool for creating materials with predictable and controlled properties, while maintaining their good processability via IPT.

4. Conclusions

In this paper, the morphology evolution of WO_X NPs has been successfully controlled by acidity level of sol-gel precursor under hydrothermal conditions. In order to evaluate EC properties of developed NPs, dual-phase films deposited *via* IPT has been investigated showing higher values of transmission modulation over the visible

and near infrared regions as compared to the poor EC performance of amorphous films. Films containing synthesized NPs exhibit 2.5 times higher optical modulation, and 2 times faster coloration time, when comparing with pure amorphous film. Such improvement is mainly attributed to the increased hydration of the structure, and higher interface between amorphous and nanocrystalline phase, as well as between WO_X layer and ion conductor. Moreover, the presence of orthorhombic NPs improves kinetics of intercalation and deintercalation mechanisms and significantly reduces the deleterious site saturation effect improving reversibility of EC action. The conductive network of interconnected WO_X NPs facilitates charge transport in the EC layer and increases significantly the active surface area of the amorphous matrix. Therefore, the impact of synthesized NPs structure and morphology on EC performance has been identified as crucial. These results demonstrate that combination of IPT with controlled synthesis of NPs provide an excellent method for the production of inorganic chromogenic films with controlled composition and dual-phase microstructure for a low temperature, direct-write fabrication of high-performance EC devices. It is evident that described approach not only leads to a significant improvement in EC performance, but also meets the challenges encountered when using synthesized WO_X NPs in a printing process. By following the presented strategy for EC tungsten oxide, it is possible to correlate the synthesis parameters with further technological processes leading to the application of those nanomaterials in high-performance electrochemical devices.

Presented engineering rules for NPs synthesis and ink formulation have to a large extend, universal character and may be implemented to other electrochemically active inkjet printed films used as *e.g.* counter electrodes, cathodes in thin film batteries, sensing films, etc. The versatility of this approach makes it a useful guide in the development of materials with predictable and controlled properties while maintaining their good processability via IPT.

Acknowledgements

This work was funded by the Portuguese Science Foundation (FCT-MEC) through project Electra, PTDC/CTM/099124/2008, EXCL/CTM-NAN/0201/2012, Strategic Project PEst-C/CTM/LA0025/2013-14 and the PhD grants SFRH/BD/45224/2008 given to P. J. Wojcik and SFRH/BD/73810/2010 given to L. Santos. Moreover, this work was also supported by E. Fortunato's ERC 2008 Advanced Grant (INVISIBLE contract number 228144), "APPLE" FP7-NMP-2010-SME/262782-2, "SMART-EC" FP7-ICT-

2009.3.9/258203 and "POINTS" FP7-NMP-263042. Authors would also like to acknowledge www.keepcalmandpublishpapers.com video blog.

Address

CENIMAT/I3N, Departamento de Ciência dos Materiais, Faculdade de Ciências e Tecnologia, FCT, Universidade Nova de Lisboa (UNL), 2829-516 Caparica, Portugal,
Fax: (+351) 21 294 8558
Tel: (+351) 21 294 8562
E-mail: p.wojcik@campus.fct.unl.pt, emf@fct.unl.pt

References

1. J. Wang, E. Khoo, P. S. Lee, and J. Ma, *J. Phys. Chem. C*, 2009, **113**, 9655–9658.

2. L. Zhou, J. Zou, M. Yu, P. Lu, J. Wei, Y. Qian, Y. Wang, and C. Yu, *Cryst. Growth Des.*, 2008, **8**, 3993–3998.

3. E. Khoo, P. S. Lee, and J. Ma, *J. Eur. Ceram. Soc.*, 2010, **30**, 1139–1144.

4. Z. Jiao, X. W. Sun, J. Wang, L. Ke, and H. V. Demir, *J. Phys. D. Appl. Phys.*, 2010, **43**, 285501.

5. J. Wang, P. S. Lee, and J. Ma, *Cryst. Growth Des.*, 2009, **9**, 2293–2299.

6. S. Songara, V. Gupta, M. Kumar Patra, J. Singh, L. Saini, G. Siddaramana Gowd, S. Raj Vadera, and N. Kumar, *J. Phys. Chem. Solids*, 2012, **73**, 851–857.

7. S. J. Hong, H. Jun, P. H. Borse, and J. S. Lee, *Int. J. Hydrogen Energy*, 2009, **34**, 3234–3242.

8. K. Huang, Q. Pan, F. Yang, S. Ni, X. Wei, and D. He, *J. Phys. D. Appl. Phys.*, 2008, **41**, 155417.

9. H. Zhang, T. Liu, L. Huang, W. Guo, D. Liu, and W. Zeng, *Phys. E Low-dimensional Syst. Nanostructures*, 2012.

10. S. Liu, F. Zhang, H. Li, T. Chen, and Y. Wang, *Sensors Actuators B Chem.*, 2012, **162**, 259–268.

11. A. Yan, C. Xie, D. Zeng, S. Cai, and H. Li, *J. Alloys Compd.*, 2010, **495**, 88–92.

12. L. Santos, J. P. Neto, A. Crespo, D. Nunes, N. Costa, I. M. Fonseca, P. Barquinha, L. Pereira, J. Silva, R. Martins, and E. Fortunato, *ACS Appl. Mater. Interfaces*, 2014, **6**, 12226–34.

13. H. Zheng, J. Z. Ou, M. S. Strano, R. B. Kaner, A. Mitchell, and K. Kalantar-zadeh, *Adv. Funct. Mater.*, 2011, 1–22.

14. D. J. Ham, A. Phuruangrat, S. Thongtem, and J. S. Lee, *Chem. Eng. J.*, 2010, **165**, 365–369.

15. R. Huang, Y. Shen, L. Zhao, and M. Yan, *Adv. Powder Technol.*, 2012, **23**, 211–214.

16. A. Phuruangrat, D. J. Ham, S. J. Hong, S. Thongtem, and J. S. Lee, *J. Mater. Chem.*, 2009, **20**, 1683–1690.

17. R. Huirache-Acuña, F. Paraguay-Delgado, M. a. Albiter, J. Lara-Romero, and R. Martínez-Sánchez, *Mater. Charact.*, 2009, **60**, 932–937.

18. S. Balaji, Y. Djaoued, A.-S. Albert, R. Z. Ferguson, and R. Brüning, *Chem. Mater.*, 2009, **21**, 1381–1389.

19. L. Jiayin, H. Jianfeng, W. Jianpeng, C. Liyun, and K. Yanagisawa, *Ceram. Int.*, 2012, **38**, 4495–4500.

20. J. Wang, P. Lee, and J. Ma, *J. Cryst. Growth*, 2009, **311**, 316–319.

21. O. Yayapao, T. Thongtem, A. Phuruangrat, and S. Thongtem, *J. Alloys Compd.*, 2011, **509**, 2294–2299.

22. J. Sungpanich, T. Thongtem, and S. Thongtem, *Ceram. Int.*, 2012, **38**, 1051–1055.

23. D. J. Taylor, J. P. Cronin, L. F. Allard, and D. P. Birniem, *Chem. Mater.*, 1996, **8**, 1396–1401.

24. M. Deepa, A. Srivastava, T. Saxena, and S. Agnihotry, *Appl. Surf. Sci.*, 2005, **252**, 1568–1580.

25. M. Deepa, M. Kar, and S. A. Agnihotry, *Thin Solid Films*, 2004, **468**, 32–42.

26. P. J. Wojcik, A. S. Cruz, L. Santos, L. Pereira, R. Martins, and E. Fortunato, *J. Mater. Chem.*, 2012, **22**, 13268.

27. I. Bernacka-Wojcik, R. Senadeera, P. J. Wojcik, L. B. Silva, G. Doria, P. Baptista, H. Aguas, E. Fortunato, and R. Martins, *Biosens. Bioelectron.*, 2010, **25**, 1229–34.

28. J. Jiang, Y. Li, J. Liu, X. Huang, C. Yuan, and X. W. D. Lou, *Adv. Mater.*, 2012, **24**, 5166–80.

29. P. M. Woodward, A. W. Sleight, and T. Vogt, *J. Solid State Chem.*, 1997, **131**, 9–17.

30. K. Yamanaka, H. Oakamoto, H. Kidou, and T. Kudo, *Jpn. J. Appl. Phys.*, 1986, **25**, 1420–1426.

31. M. Law, L. E. Greene, J. C. Johnson, R. Saykally, and P. Yang, *Nat. Mater.*, 2005, **4**, 455–9.

32. P. C. Barbosa, L. C. Rodrigues, M. M. Silva, M. J. Smith, P. B. Valente, A. Gonçalves, and E. Fortunato, *Polym. Adv. Technol.*, 2011, **22**, 1753–1759.

33. A. Al Mohammad, *Acta Phys. Pol. A*, 2009, **116**, 240–244.

34. B. Pecquenard, S. Castro-Garcia, J. Livage, P. Y. Zavalij, M. S. Whittingham, and R. Thouvenot, *Chem. Mater.*, 1998, **10**, 1882–1888.

35. J. Wang, E. Khoo, P. S. Lee, and J. Ma, *J. Phys. Chem. C*, 2008, **112**, 14306–14312.

36. H. S. Khoo, C. Lin, S.-H. Huang, and F.-G. Tseng, *Micromachines*, 2011, **2**, 17–48.

37. Y. Huang, X. Duan, Q. Wei, and C. M. Lieber, *Science*, 2001, **291**, 630–3.

38. S. Mueller, E. W. Llewellin, and H. M. Mader, *Proc. R. Soc. A*, 2009, **466**, 1201–1228.

39. C. G. Granqvist, *Sol. Energy Mater. Sol. Cells*, 2000, **60**, 201–262.

40. Y. Krasnov, *Electrochim. Acta*, 2004, **49**, 2425–2433.

41. B. W. Faughnan, R. S. Crandall, and M. A. Lampert, *Appl. Phys. Lett.*, 1975, **27**, 275–277.

42. P. M. Kadam, N. L. Tarwal, P. S. Shinde, R. S. Patil, A. K. Bhosale, H. P. Deshmukh, and P. S. Patil, *J. Alloys Compd.*, 2010, 3–7.

43. B. Yebka, B. Pecquenard, C. Julien, and J. Livage, *Solid State Ionics*, 1997, **104**, 169–175.

44. S.-I. Pyun and J.-S. Bae, *J. Alloys Compd.*, 1996, **245**, L1–L4.

45. M. Denesuk and D. R. Uhlmann, *J. Electrochem. Soc.*, 1996, **143**, L186–L188.

Table of contents entry

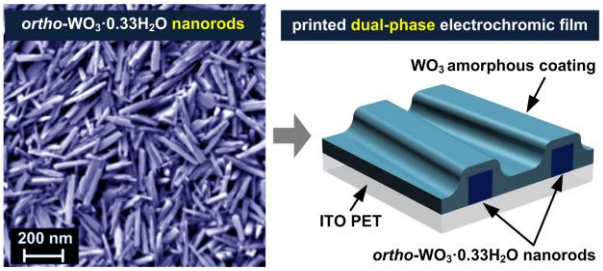

We demonstrate engineering procedures governing the development of inkjet printable metal oxide nanoparticles for electrochromic applications with effectively improved opto-electrochemical response.